Nanoscale Metal-Organic Layers for Deeply Penetrating X-ray Induced Photodynamic Therapy

Guangxu Lan[‡,a], **Kaiyuan Ni**[‡,a], **Ruoyu Xu**[a], **Kuangda Lu**[a], **Zekai Lin**[a], **Christina Chan**[a], and **Wenbin Lin**[a]

[a]Department of Chemistry, The University of Chicago 929 East 57th street, Chicago, Illinois 60637, United States

Abstract

We report the rational design of metal-organic layers (MOLs) that are built from $[Hf_6O_4(OH)_4(HCO_2)_6]$ secondary building units (SBUs) and $Ir[bpy(ppy)_2]^+$- or $Ru(bpy)_3^{2+}$-derived tricarboxylate ligands (Hf-BPY-Ir or Hf-BPY-Ru; bpy = 2,2′-bipyridine, ppy = 2-phenylpyridine) and their applications in X-ray induced photodynamic therapy (X-PDT) of colon cancer. Heavy Hf atoms in the SBUs efficiently absorb X-rays and transfer energy to $Ir[bpy(ppy)_2]^+$ or $Ru(bpy)_3^{2+}$ moieties to induce PDT by generating reactive oxygen species (ROS). The ability of X-rays to penetrate deeply into tissue and efficient ROS diffusion through ultrathin 2-D MOLs (~1.2 nm) enable highly effective X-PDT to afford superb anticancer efficacy.

Graphical abstract
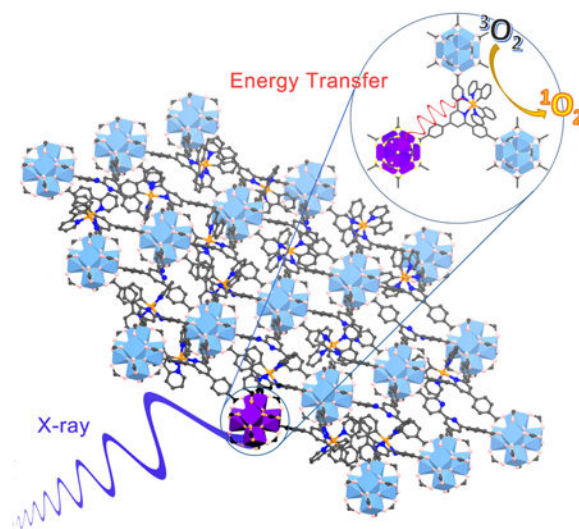
X-ray induced PDT: Heavy Hf atoms in the SBUs efficiently absorb X-rays and transfer energy to $Ir[bpy(ppy)_2]^+$ or $Ru(bpy)_3^{2+}$ moieties in ultrathin metal-organic layers to induce PDT by generating reactive oxygen species (ROS). Deep tissue penetration of X-rays, high $^1O_2$ quantum

yields, and efficient ROS diffusion allow for regression of colorectal tumors via MOL-mediated, X-ray induced PDT treatments.

Keywords

Nanoscale Metal-Organic Layer; Photodynamic Therapy; X-ray; Cancer Treatment

By combining three intrinsically nontoxic components--a photosensitizer (PS), light, and tissue oxygen--to generate cytotoxic reactive oxygen species (ROS), particularly singlet oxygen ($^1O_2$), photodynamic therapy (PDT) provides a highly effective phototherapy against cancer.[1] Because ROS indiscriminately kill both diseased and normal cells, it is critical to selectively localize PSs in tumors in order to enhance PDT efficiency and minimize collateral damage to normal tissues.[2-13] We and others reported a series of porphyrin-and chlorin-based nanoscale metal-organic frameworks (nMOFs) as PSs for effective PDT.[14-19] Because the lifetime of ROS is short, it is not feasible for all the species generated to diffuse out of the 3-D structure of nMOFs to exert cytotoxicity on cellular organelles, thus limiting the overall efficacy of PDT *in vivo*.

We hypothesized that the *in vivo* PDT efficacy of nMOFs could be further improved by reducing the dimensionality to afford 2-D metal-organic layers (MOLs) and exciting the MOLs with more tissue-penetrating X-rays. We recently reported a new class of tunable and functionalizable MOLs that are composed of $[Hf_6O_4(OH)_4(HCO_2)_6]$ secondary building units (SBUs) and benzene-1,3,5-tribenzoate (BTB) bridging ligands.[20] The 2-D structure of MOLs allow s ROS to diffuse freely, thus presenting an ideal platform for designing nanoscale PSs for efficient PDT.

Ir[bpy(ppy)$_2$]$^+$ (bpy = 2,2′-bipyridine, ppy = 2-phenylpyridine) and Ru(bpy)$_3^{2+}$ are two efficient PSs with the very high $^1O_2$ quantum yields (Φ) of 0.97 and 0.73, respectively.[21-23] However, due to large Stoke shifts, they can only be excited with photons at short wavelengths, ~355 nm for Ir[bpy(ppy)$_2$]$^+$ and ~450 nm for Ru(bpy)$_3^{2+}$. Such UV-Vis photons cannot penetrate human tissue (penetration depth <0.1 mm),[24] which severely limits their application in PDT. Our previous work demonstrated that a Hf-based nMOF can absorb X-rays and transfer energy to coordinated anthracene-based ligands to luminesce in the visible spectrum.[25] We believe that coordination between Ir[bpy(ppy)$_2$]$^+$- or Ru(bpy)$_3^{2+}$-derived tricarboxylate ligands and heavy Hf-based SBUs would enable direct excitation of the PSs by X-rays to achieve X-ray induced photodynamic therapy (X-PDT).[26] Here we report the rational design of two MOLs, composed of $[Hf_6O_4(OH)_4(HCO_2)_6]$ SBUs and Ir[bpy(ppy)$_2$]$^+$- or Ru(bpy)$_3^{2+}$-derived tricarboxylate ligands, as potent PSs. The Hf-MOLs achieve greatly enhanced PDT efficacy both *in vitro* and *in vivo* upon X-ray irradiation.

Hf-BPY-Ir and Hf-BPY-Ru MOLs were synthesized by a postsynthetic metalation method. 4′,6′-dibenzoato-[2,2′-bipyridine]-4-carboxylic acid (H$_3$BPY) was synthesized as show n in Figure S1 (SI) and treated with HfCl$_4$ in N,N-dimethylformamide (DMF), formic acid, and water to afford Hf-BPY MOL as a white precipitate, which was then washed twice with DMF and once with ethanol. By optimizing the amounts of formic acid and H$_2$O, the size of

Hf-BPY could be controlled to a diameter of ~500 nm, as verified by transmission electron microscopy (TEM) (Figure 1a). Hf-BPY was treated with $[Ir(ppy)_2Cl]_2/Ru(bpy)_2Cl_2$ to afford Hf-BPY-Ir/Hf-BPY-Ru MOL as an orange/brow n participate. Due to the 2-D structure of Hf-BPY, the bpy coordination sites are highly accessible, resulting in efficient metalation. The Ir and Ru loadings were determined to be 67% and 59% for Hf-BPY-Ir and Hf-BPY-Ru, respectively, as determined by Inductively Coupled Plasma-Mass Spectrometry (ICP-MS).

In Hf-BPY, each Hf_6 cluster of 12-connectivity was capped by 6 formate groups (three at the top and three at the bottom), leaving the remaining six sites coordinated to 3-connected BPY ligands to form a 3,6-connected 2-D network of $Hf_6(\mu_3-O)_4(\mu_3-OH)_4(HCO_2)_6(BPY)_2$ of kagome dual (kgd) topology (Scheme 1). High-resolution TEM (HRTEM) images of Hf-BPY, where Hf_6 clusters appear as dark spots, and fast Fourier transform (FFT) patterns (Figure 1b) of Hf-BPY were consistent with the kgd topology. The distance between two adjacent dark spots in the HRTEM was 2.0 nm, which matched the distance between two adjacent SBUs. The powder X-ray diffraction (PXRD) pattern of Hf-BPY was identical to that of the Hf-BTB MOL (Figure 2a),[20] which further confirmed the kgd structure of Hf-BPY. Atomic force microscopy (AFM) images (Figure 1e, 1f and S13) of Hf-BPY showed a 1.2 nm thickness, which is very close to the van der Waals size of the Hf_6 cluster capped by formate groups, indicating the monolayer structure of Hf-BPY. A nitrogen sorption study of Hf-BPY gave a BET surface are of 346 m^2/g (Figure S15), indicating its porous structure. The ultrathin monolayer structure facilitates the diffusion of $^1O_2$ as its diffusion length was estimated to be 20-220 nm in cells.[27]

TEM imaging showed that Hf-BPY-Ir (Figure 1c) and Hf-BPY-Ru (Figure 1d) have similar morphologies and sizes as Hf-BPY. The retention of the MOL structure after metalation was supported by the similarity among the PXRD patterns of Hf-BPY-Ir, Hf-BPY-Ru, and Hf-BPY (Figure 2a). In addition, the HRTEM images and FFT patterns of Hf-BPY-Ir and Hf-BPY-Ru (Figure S10) were identical to those of Hf-BPY. TEM images and PXRD patterns of the MOLs remained unchanged after incubation in DMEM media for 12 h (Figures S16 and 17), suggesting that the MOLs are stable for biomedical applications.

To further confirm the metalation of Hf-BPY and to understand the coordination environments of Ir and Ru centers in Hf-MOLs, we synthesized $[(H_3BPY)Ir(ppy)_2]$ Cl (H_3BPY-Ir) and $[(H_3BPY)Ru(bpy)_2]$ Cl_2 (H_3BPY-Ru) as ligand controls (Figure S6-S9). The UV-visible absorption spectra of Hf-based MOLs exhibit similar MLCT bands as their corresponding ligands (Figure 2b). Importantly, X-ray absorption spectroscopy (XAS) indicated that Zr-BPY-Ir and Hf-BPY-Ru have the same Ir and Ru coordination environments as H_3BPY-Ir and H_3BPY-Ru, respectively (Figure S20-S23). Due to similar energy between Ir L_3-edge (11215 eV) and Hf L_1-dege (11271 eV), XAS data was collected for Zr-BPY-Ir instead of Hf-BPY-Ir.

We next examined singlet oxygen generation efficiencies of MOLs using 4-nitroso-N,N-dimethylanaline (RNO) assay. We also synthesized Zr-MOLs (Zr-BPY-Ir and Zr-BPY-Ru) using similar processes (Figure S11 and S12) and used them for comparison. Upon irradiation with a Xe lamp using a 400 nm long-pass filter or X-rays (225 KVp, 13 mA),

the $^1O_2$ generated by MOLs reacted with RNO in the presence of histidine, leading to a decrease of absorbance at 440 nm in the UV-visible spectra (Figure S24 and S25). By linearly fitting difference in RNO peak absorbance [(OD)] against irradiation doses (which scale linearly with exposure times upon visible light or X-ray dose, Y = Ax + B), the RNO assay provides a quantitative measure of $^1O_2$ generation efficiencies, with a more positive slope indicating more efficient $^1O_2$ generation. Upon visible light irradiation, the linear fitting results showed that Ir-based Zr- and Hf-MOLs generated $^1O_2$ more efficiently than Ru-based Zr- and Hf-MOLs (Figures 2c, Table S3), consistent with the difference in $^1O_2$ generation quantum yields between $[Ir(bpy)(ppy)_2]^+$ ($\varphi = 0.97$) and $[Ru(bpy)_3]^{2+}$ ($\varphi = 0.73$). Furthermore, only very slight differences were observed between two Ir-based MOLs (A = 1.09×10^{-2} for Hf-BPY-Ir and A = 0.88×10^{-2} for Zr-BPY-Ir) or two Ru-based MOLs (A = 4.1×10^{-3} for Hf-BPY-Ru and A = 2.4×10^{-3} for Zr-BPY-Ru), suggesting minor effects of the SBUs in the $^1O_2$ generation efficiency through spin-orbit coupling. [14,28] The efficient singlet oxygen generation by Hf-BPY-Ir upon light irradiation was also demonstrated by Singlet Oxygen Sensor Green (SOSG) assay (Figure S26). Comparisons with DBP-Hf, a porphyrin-based nMOF reported by us previously, indicated that Hf-BPY-Ir is more effective in generating $^1O_2$ than DBP-Hf upon light irradiation (Figure S27), suggesting the facile diffusion of ROS through the MOL monolayer.

However, upon X-ray irradiation, there was a drastic difference in $^1O_2$ generation efficiencies in Zr- and Hf-MOLs (Figure 2d, Table S4). Both Hf-MOLs (A = 1.22×10^{-2} for Hf-BPY-Ir and A = 1.0×10^{-2} for Hf-BPY-Ru) possessed much higher $^1O_2$ generation efficiency than their corresponding Zr-MOLs (A = 0.39×10^{-2} for Hf-BPY-Ir and A = 0.19×10^{-2} for Zr-BPY-Ir), supporting our hypothesis that the X-ray energy was first absorbed by SBUs and then transferred to the PSs in the bridging ligands to lead to the X-PDT effect. Because the heavier Hf atoms absorb X-rays more efficiently than the Zr atoms, the Hf-MOLs are expected to be more effective at X-PDT Additionally, Ir-based MOLs showed only slightly better X-PDT efficiency than Ru-based MOLs, suggesting different energy transfer processes involved in X-PDT and PDT

In the clinic, PDT is typically applied to superficial malignant tumors such as skin lesions and esophageal cancer due to the limited penetration of light (~3 mm at 800 nm). We sought to examine the potential of MOL-mediated X-PDT in the treatment of deeply seated tumors. Two types of murine colon adenocarcinoma cells, CT26 and MC38, were used for *in vitro* and *in vivo* studies. The cellular uptake was evaluated on CT26 cells incubated with Hf-BPY-Ir, Hf-BPY-Ru, or Hf-BPY at a Hf concentration of 50 μM for 1, 4, 8, and 24 h. At each time point, cells were digested and the Hf contents were determined by ICP-MS. Hf-BPY-Ru showed higher uptake (6580 ± 1770 ng/10^5 cells) than Hf-BPY-Ir (3317 ± 665 ng/10^5 cells) and Hf-BPY (1930 ± 716 ng/10^5 cells), presumably because of the higher positive charge of Hf-BPY-Ru, which favors interacting with the negatively charged cell membrane to facilitate endocytosis (Figure S28).

We next investigated the *in vitro* anticancer efficacy of three different Hf-based MOLs against CT26 (Figure 3a) and MC38 (Figure 3b) cells. To elucidate the key role of Hf in efficient absorption of X-rays, three corresponding Zr-MOLs were used as controls. MOLs were incubated with cells at various concentrations for 8 h, followed by irradiation with an

X-ray irradiator at a dose of 2 Gy. Hf-BPY-Ir and Hf-BPY-Ru outperformed Hf-BPY and three Zr-MOLs. The IC$_{50}$ values for Hf-BPY-Ir, Hf-BPY-Ru, and Hf-BPY against CT26 cells were calculated to be 3.82 ± 1.80, 3.63 ± 2.75, and 24.90 ± 7.87 μM, respectively. Against MC38 cells, the IC$_{50}$ values were 11.66 ± 1.84, 10.72 ± 2.92, and 37.80 ± 6.57 μM, respectively. IC$_{50}$ values exceeded 100 μM for Zr-BPY-Ir, Zr-BPY-Ru, and Zr-BPY in both CT26 and MC38 cell lines. No cytotoxicity was observed in dark control groups (Figure S29). We also tested cell viability with fixed Hf-MOL concentrations based on Ir, Ru, or BPY of 20μM, respectively, and various X-ray doses (Figure S30). All of the results showed greatly enhanced X-PDT potency of Ir[bpy(ppy)$_2$]$^+$ and [Ru(bpy)$_3$]$^{2+}$ in Hf-MOLs. Importantly, X-ray induced cytotoxicity of Hf-BPY-Ir and Hf-BPY-Ru remained essentially unchanged when the cells were covered with a beef block of 1 cm in thickness during X-ray irradiation (Figure S41). In contrast, light induced cytotoxicity of Hf-BPY-Ir and Hf-BPY-Ru was completely lost when the cells were covered with the same beef block during light irradiation (Figure S40). These results support our hypothesis that MOL-mediated X-PDT can be used to treat deep-seated tumors. Interestingly, control experiments with Hf-QPDC-Ir nMOF, a UiO nMOF built from Hf$_6$(μ$_3$-O)$_4$(μ$_3$-OH)$_4$ SBUs and QPDC-Ir bridging ligands, further support the enhanced X-PDT efficacy of the MOLs due to facile ROS diffusion; upon X-ray irradiation, Hf-QPDC-Ir nMOF exhibited much higher IC$_{50}$ values of 32.85 ± 3.02μM for CT26 cells and 26.08 ± 2.38 μM for MC38 cells, respectively (Figure S39).

We then explored the mechanism of X-ray induced cytotoxicity on CT26 cells. ^{1}O$_2$ generation in live cells was examined by SOSG and detected by confocal laser scanning microscopy (CLSM) (Figure S31). After preloading cells with SOSG and incubating them with PBS, Hf-MOLs, or H$_3$BPY ligand for 8 h at a concentration of 20 μM based on Ir, Ru, or BPY, respectively, they were irradiated with X-rays at a dose of 2 Gy, immediately followed by CLSM imaging. Both Hf-BPY-Ir-and Hf-BPY-Ru-treated cells showed strong green SOSG fluorescence, indicating the efficient generation of ^{1}O$_2$ in the MOLs upon X-ray irradiation. In contrast, PBS, Hf-BPY and H$_3$BPY ligand-treated groups showed no SOSG signal after X-ray induced ^{1}O$_2$ generation, which supported our proposed X-PDT process using Hf-BPY-Ir and Hf-BPY-Ru MOLs. We also performed γ-H$_2$AFX assay (Life technology, USA) on CT26 cells to determine DNA double-strand breaks (DSBs) caused by MOLs upon X-ray irradiation. As shown in Figure S37, CT26 cells treated with three Hf-based MOLs showed significant red fluorescence, indicating DSBs induced by hydroxyl radical from X-ray irradiation. This result suggests that Hf$_6$ SBUs are capable of radiosensitization to further enhance cytotoxicity of MOL-mediated X-PDT.

Encouraged by *in vitro* results, we carried out *in vivo* anticancer efficacy experiments on subcutaneous flank tumor-bearing mouse models of CT26 and MC38. When tumors reached 100-150 mm^3 in volume, Hf-BPY-Ir, Hf-BPY-Ru, or Hf-BPY with amount of 0.5 nmol based on Ir, Ru or BPY, respectively, or PBS was intratumorally injected followed by daily X-ray irradiation at a dose of 1 Gy/fraction (120 kVp, 20 mA, 2 mm-Cu filter) for a total of 5 fractions on the CT26 model (Figure 3c) or 10 fractions on the MC38 model (Figure 3d) on consecutive days. Tumor sizes and body weights were measured every day. All mice were sacrificed 18 days after tumor inoculation, and the excised tumors were photogaphed and weighed (Figure S33-S34). To rule out any radiotherapy effects from the low dose X-ray, we used PBS-treated mice without X-ray irradiation as a dark control. The PBS groups with or

without irradiation did not show any difference in tumor growth curves, indicating that low dose X-rays alone had no radiotherapeutic effects. The Hf-BPY goups appeared to show slight inhibition of tumor growth (P=0.047 or 0.048 for CT26 or MC38, respectively), consistent with the radiosensitization effects of the Hf_6 SBUs. In stark contrast, Hf-BPY-Ir and Hf-BPY-Ru treatments led to effective tumor regression in CT26 with 5 fractions of X-ray irradiation (5 Gy total; total volume reduction of 83.6% or 77.3%, respectively) and in MC38 with 10 fractions of X-ray irradiation (10 Gy; total total volume reduction of 82.3% or 90.1%, respectively). The weights and sizes of tumors treated with Hf-BPY-Ir and Hf-BPY-Ru at the end point were significantly smaller than the other groups (Table S5 and S6). Histology of frozen tumor slices confirmed MOL-assisted X-PDT caused apoptosis/necrosis in tumors (Figure S35). No abnormalities were observed on histological images of frozen organ slices, which indicated that X-PDT with intratumoral injection of MOLs was not systemically toxic (Figure S36). The lack of systemic toxicity was further supported by steady body weights and similar weight gain patterns in all groups (Figure S32).

In summary, we rationally designed and synthesized two Hf-MOLs as powerful PSs for effective X-PDT of colon cancer models. Upon X-ray irradiation, Hf atoms in the SBUs absorb X-rays and transfer energy to $Ir[bpy(ppy)_2]^+$ or $[Ru(bpy)_3]^{2+}$ in the ligands to generate $^1O_2$, demonstrated by both RNO assay and *in vitro* $^1O_2$ detection as well as cytotoxicity studies. As a result of deep tissue penetration of X-rays, high $^1O_2$ quantum yields of $Ir[bpy(ppy)_2]^+$ or $[Ru(bpy)_3]^{2+}$, and efficient ROS diffusion through ultrathin MOLs, X-PDT treatment led to an impressive 90% reduction in tumor volumes. MOLs thus represent a novel class of 2-D materials with great potential for cancer treatment and other biomedical applications.

Supplementary Material

Refer to Web version on PubMed Central for supplementary material.

Acknowledgments

References

1. Celli JP, Spring BQ, Rizvi I, Evans CL, Samkoe KS, Verma S, Pogue BW, Hasan T. Chem Rev. 2010; 110:2795. [PubMed: 20353192]

2. Bechet D, Couleaud P, Frochot C, Viriot ML, Guillemin F, Barberi-Heyob M. Trends biotechnol. 2008; 26:612. [PubMed: 18804298]

3. Ng KK, Zheng G. Chem Rev. 2015; 115:11012. [PubMed: 26244706]

4. Huynh E, Leung BY, Helfield BL, Shakiba M, Gandier JA, Jin CS, Master ER, Wilson BC, Goertz DE, Zheng G. Nat Nanotechnol. 2015; 10:325. [PubMed: 25822929]

5. Carter KA, Shao S, Hoopes MI, Luo D, Ahsan B, Grigoryants VM, Song W, Huang H, Zhang G, Pandey RK. Nat Comm. 2014; 5

6. Lovell JF, Jin CS, Huynh E, Jin H, Kim C, Rubinstein JL, Chan WC, Cao W, Wang LV, Zheng G. Nat Mater. 2011; 10:324. [PubMed: 21423187]

7. Idris NM, Gnanasammandhan MK, hang JZ, Ho PC, Mahendran R, Zhang Y. Nat Med. 2012; 18:1580. [PubMed: 22983397]

8. He C, Liu D, Lin W. ACS Nano. 2015; 9:991. [PubMed: 25559017]

9. He C, Duan X, Guo N, Chan C, Poon C, Weichselbaum RR, Lin W. Nat Comm. 2016; 7

10. Cheng Y, Samia A C, Meyers JD, Panagopoulos I, Fei B, Burda C. J Am Chem Soc. 2008; 130:10643. [PubMed: 18642918]

11. Chatterjee DK, Fong LS, Zhang Y. Adv Drug Deliv Rev. 2008; 60:1627. [PubMed: 18930086]

12. Roy I, Ohulchanskyy TY, Pudavar HE, Bergey EJ, Oseroff AR, Morgan J, Dougherty TJ, Prasad PN. J Am Chem Soc. 2003; 125:7860. [PubMed: 12823004]

13. Zheng X, Wang L, Pei Q, He S, Liu S, Xie Z. Chem Mater. 2017; 29:2374.

14. Lu K, He C, Lin W. J Am Chem Soc. 2014; 136:16712. [PubMed: 25407895]

15. Lu K, He C, Lin W. J Am Chem Soc. 2015; 137:7600. [PubMed: 26068094]

16. Lu K, He C, Guo N, Chan C, Ni K, Weichselbaum RR, Lin W. J Am Chem Soc. 2016; 138:12502. [PubMed: 27575718]

17. Park J, Jiang Q, Feng D, Mao L, Zhou H. J Am Chem Soc. 2016; 138:3518. [PubMed: 26894555]

18. Liu J, Yang Y, Zhu W, Yi X, Dong Z, Xu X, hen MC, Yang K, Lu G, Jiang L, Liu Z. Biomaterials. 2016; 97:1. [PubMed: 27155362]

19. Lismont M, Dreesen L, Wuttke S. Adv Funct Mater. 2017; 27:1606314.

20. Cao L, Lin Z, Peng F, Wang W, Huang R, Wang C, Yan J, Liang J, Zhang Z, Zhang T, Long L, Sun J, Lin W. Angew Chem Int Ed. 2016; 55:4962.

21. Takizawa, Sy, Aboshi, R., Murata, S. Photochem Photobiol Sci. 2011; 10:895. [PubMed: 21298183]

22. Djurovich PI, Murphy D, Thompson ME, Hernandez B, Gao R, Hunt PL, Selke M. Dalton Trans. 2007; 34:3763.

23. Garcìa-Fresnadillo D, Georgiadou Y, Orellana G, Braun AM, Oliveros E. Helv Chim Acta. 1996; 79:1222.

24. Smith AM, Mancini MC, Nie S. Nat Nanotechnol. 2009; 4:710. [PubMed: 19898521]

25. Wang C, Volotskova O, Lu K, Ahmad M, Sun C, Xing L, Lin W. J Am Chem Soc. 2014; 136:6171. [PubMed: 24730683]

26. Chen H, Wang GD, Chuang YJ, Zhen Z, Chen X, Biddinger P, Hao Z, Liu F, Shen B, Pan Z, Xie J. Nano lett. 2015; 15:2249. [PubMed: 25756781]

27. Moan J, Berg K. Photochem photobiol. 1991; 53:549. [PubMed: 1830395]

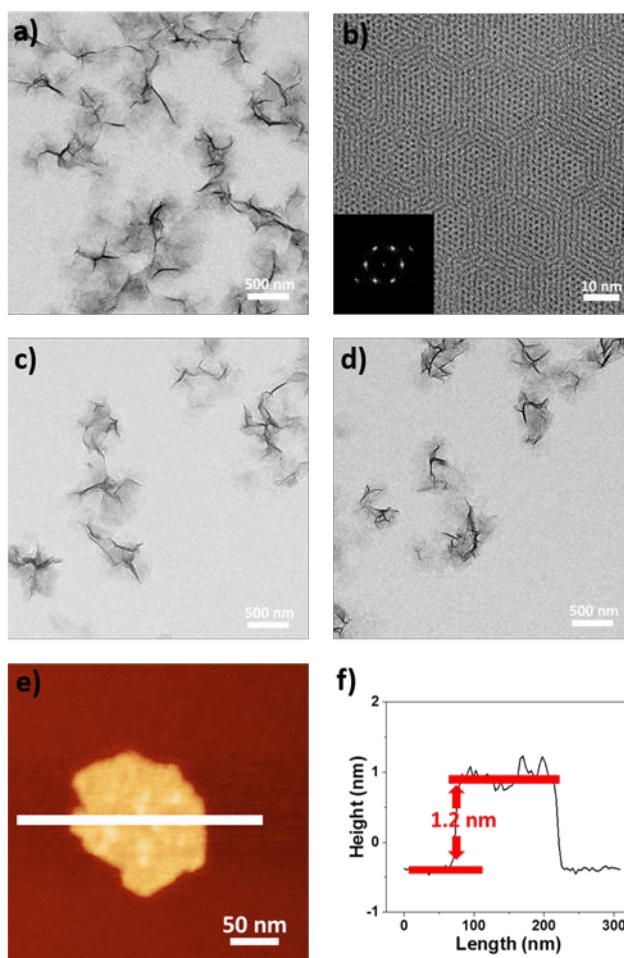28. Scandola F, Chiorboli C, Prodi A, Iengo E, Alessio E. Coord Chem Rev. 2006; 250:1471.

Figure 1.
Morphology and structure of Hf-based MOLs. TEM image (a), HRTEM image, and FFT pattern (b) of Hf-BPY. TEM images of Hf-BPY-Ir (c) and Hf-BPY-Ru (d). Tapping-mode AFM topography (e) and the height profile along the white line (f) of Hf-BPY.
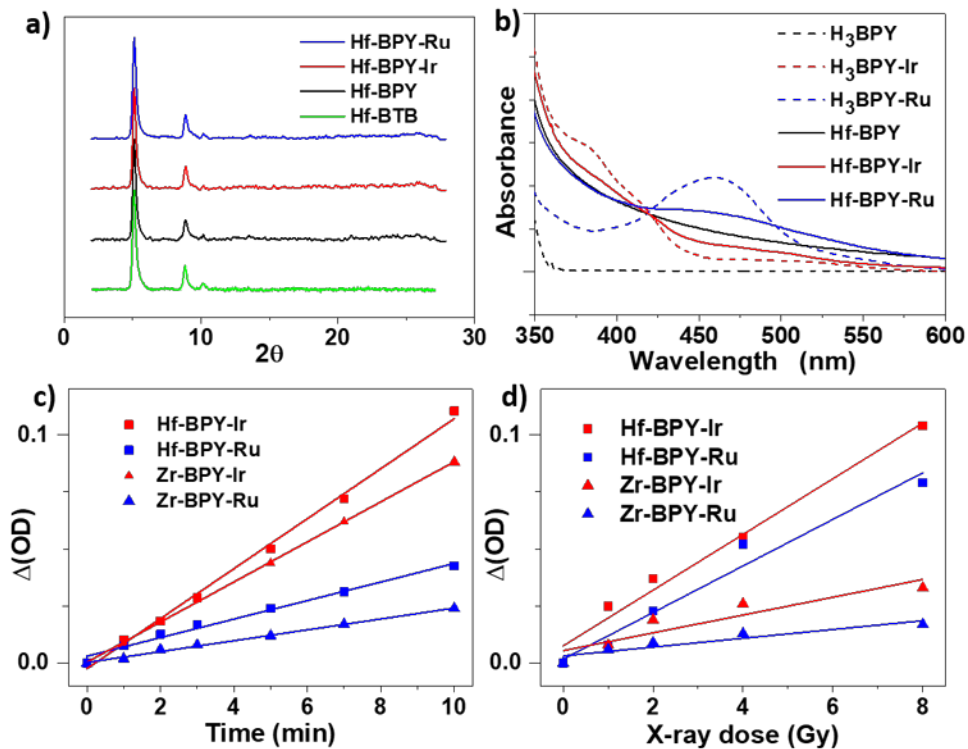
Figure 2.
(a) PXRD patterns of new Hf-MOLs and the Hf-BTB MOL. (b) UV-visible absorption spectra of Hf-MOLs and the bridging ligands. Singlet oxygen generation of Hf-and Zr-MOLs upon visible light irradiation (c) or X-ray irradiation (d), as determined by RNO. Linear fit of (OD) at 440 nm against irradiation dose.
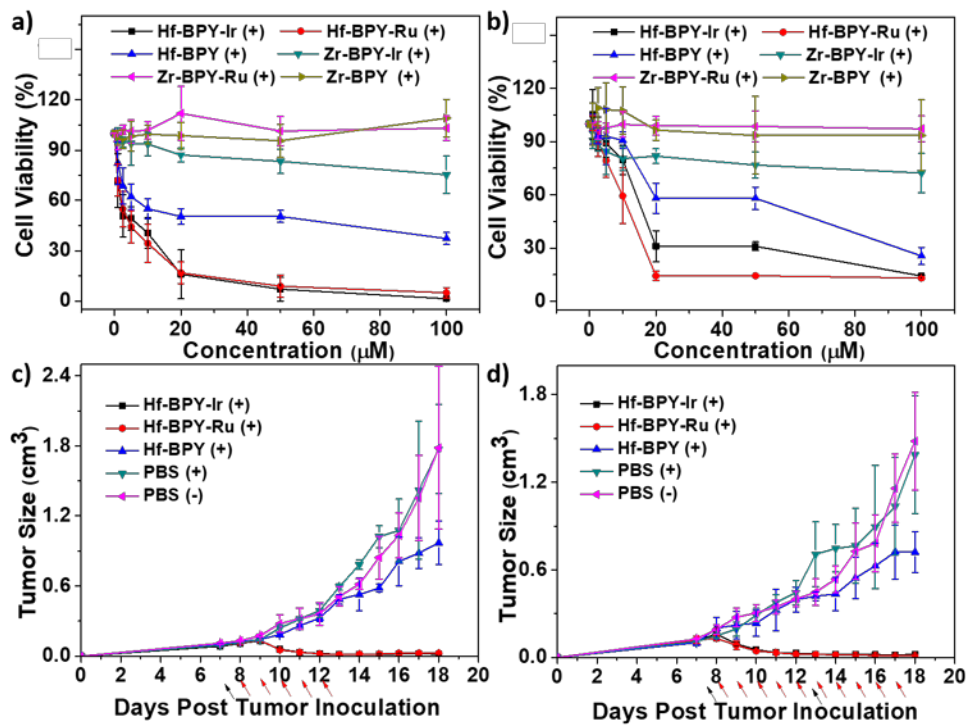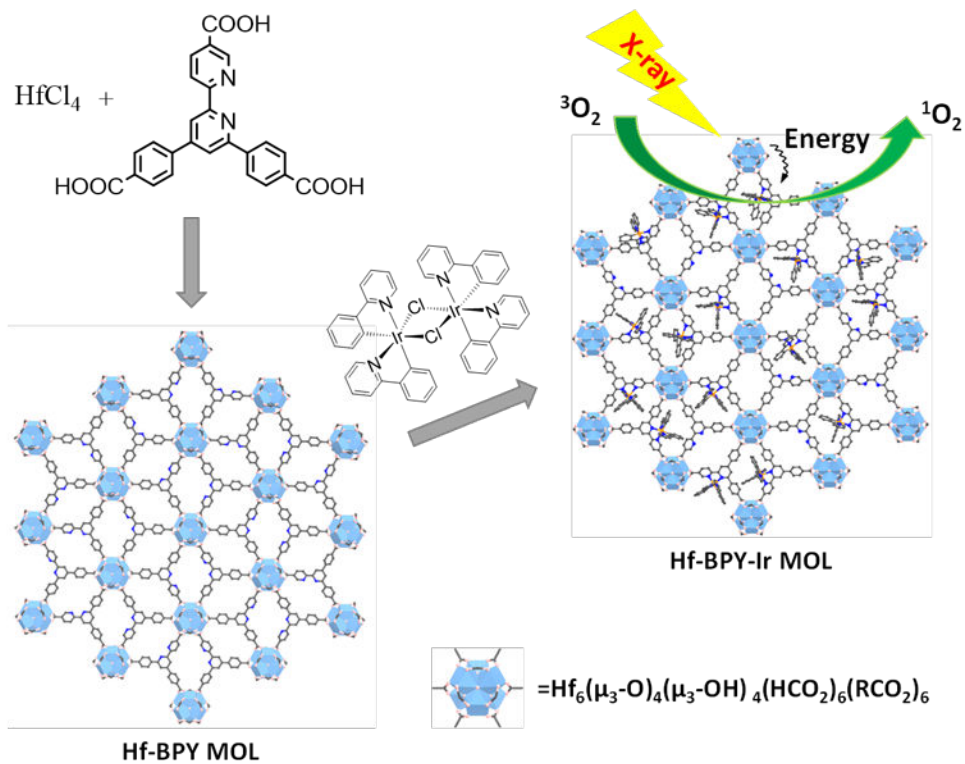
Figure 3.
In viro and *in vivo* anticancer efficacy of Hf-MOLs. Cytotoxcity of Hf- and Zr-MOLs in CT26 cells (a) and MC38 cells (b). Tumor growth inhibition curves after X-PDT treatment in the CT26 (c) and MC38 (d) models. Black arrows refer to injection of MOLs and red arrows refer to X-ray irradiation.

Scheme 1. Synthesis of Hf-based MOLs and MOL-enabled X-PDT to generate singlet oxygen